CPC(HEP & NP), 2012, **36**(10): 1013–1018 Chinese Physics C Vol. 36, No. 10, Oct., 2012

Three-dimensional particle-in-cell with Monte Carlo collision simulation of the electron energy distribution function in the multi-cusp ion source for proton therapy

YANG Chao(杨超)[1] WU Xiao-Bing(吴小兵)[2] LIU Da-Gang(刘大刚)[1]

[1] University of Electronic Science and Technology of China, Chengdu 610054, China
[2] Institute of High Energy Physics, Chinese Academy of Sciences, Beijing 100049, China

Abstract: For optimization and accurate prediction of the amount of proton production in the multi-cusp ion source, analysis of the electron energy distribution function (EEDF) is necessary. A three dimensional particle-in-cell with Monte Carlo collision (PIC-MCC) code based on the CHIPIC software platform are developed. The code is applied to the multi-cusp proton source. The results show that there are two energy distributions in the discharge chamber, and a spatial non-uniformity of electron density due to the $\vec{B}\times\nabla B$ drift of the top permanent magnets is observed.

Key words: multi-cusp proton source, EEDF, PIC-MCC

PACS: 52.65.Pp, 52.50.Dg, 29.20.Ej **DOI:** 10.1088/1674-1137/36/10/018

1 Introduction

Nowadays proton therapy has become a very important method for cancer treatment that has been verified by clinical studies worldwide. The Advanced Proton Therapy Facility (APTF) is an accelerator-based project currently proposed in China [1]. The accelerator complex consists of a 7 MeV linear accelerator as an injector and a 70–250 MeV slow cycling proton synchrotron. The linear accelerator consists of a 50 keV multi-cusp proton source driven by dual filaments, a low energy beam transport (LEBT) line, a 2.5 MeV radio frequency quadrupole (RFQ) accelerator and a 7 MeV drift tube linear (DTL) accelerator. The design of the ion source for the APTF was described previously in detail [2]. The proton therapy facility has strict requirements for the ion source's and LEBT's reliability, repetition, life time and maneuverability.The uniformity of the extraction proton beam is a very important factor for the downstream acceleration and therapy facility. The proton is produced by the collision between the electron and the hydrogen molecule. As a result, the distribution of the phase space and energy for the electron is the key factor for the proton uniformity. Based on the CHIPIC [3] software platform, a three dimensional PIC-MCC [4] code is developed. By using the PIC-MCC code, the multi-cusp proton source is studied.

The schematic of a multi-cusp proton source discharge chamber and extraction system is shown in Fig. 1. The chamber mainly consists of a stainless

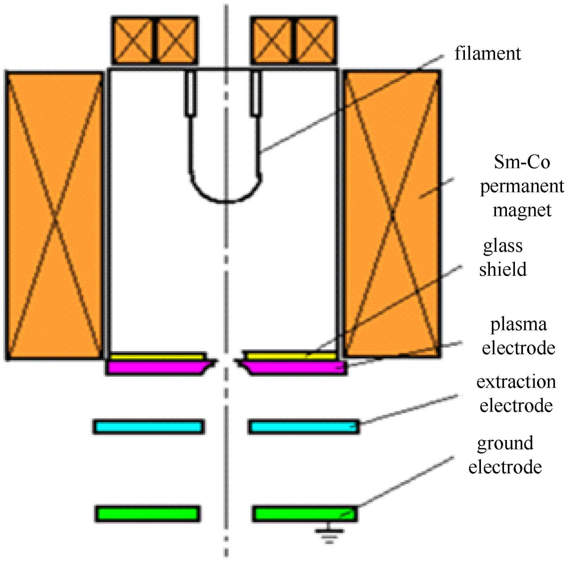

Fig. 1. The schematic of a multi-cusp proton source discharge chamber and extraction system.

Received 5 January 2012

steel source body, two filaments, several Sm-Co permanent magnets, and a glass shield which is used to enhance the plasma density and proton content. The extraction system contains a plasma electrode, an extraction and a grounded electrode.

2 Basic equations and numerical techniques

2.1 PIC-MCC algorithm

The general flow of the PIC-MCC scheme is shown schematically in Fig. 2 [5].

As shown in Fig. 2, in the PIC-MCC scheme, firstly the particle equations of motion are integrated; secondly, the boundary conditions are dealt with; thirdly, the electromagnet field equations on a grid are integrated; fourthly, the field is coupled to the particles; and finally Monte Carlo collisions of the motions, and then the whole process is repeated again.

In order to calculate the EEDF in the ion source, the equation of the motion for electrons is solved directly.

$$m_{\mathrm{e}}\frac{\mathrm{d}\vec{v}}{\mathrm{d}t}=e(\vec{E}+\vec{v}\times\vec{B})+(\text{collisionterm}), \qquad (1)$$

where the m_{e} is the mass, $\vec{v}$ is the velocity, e is the electric charge of an electron, $\vec{E}$ is the electric, and $\vec{B}$ is the magnetic field.

The equation of motion is numerically solved by the Boris-Buneman version of the leap-frog method [6]. Various collision processes are taken into account in Eq. (1) by using Monte Carlo techniques. They are classified mainly into two categories [7]. The first one is the Coulomb collision between electrons, which is treated with the “binary collision (BC)” model [8]. The second one is the collisions between the electrons and the hydrogen species, which are treated with the “null-collision (NC)” method [9]. Hundreds of collision processes are included in the analysis. Among these processes, the main collision species are summarized in Table 1.

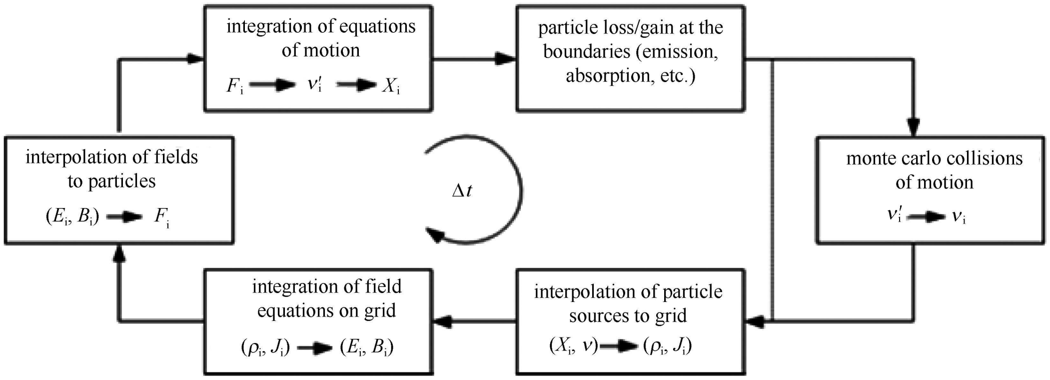

Fig. 2. Flow schematic for the PIC-MCC scheme.

Table 1. The main collision processes included in the simulation.

index	collision species	before	after
1	excitation	e+H(1s)	e+H*(2p)
2	ionization	e_1+ H(1s)	e_1+e_2+H$^+$
3	vibrational excitation	e+H$_2$(v=0)	e+H$_2$(v=1)
4	electronic excitation	e+ H$_2$(X $^1\sum_g^+$)	e+ H$_2^*$(B $^1\sum_u^+$2pσ)
5	electronic excitation	e+H$_2$(X $^1\sum_g^+$)	e+H$_2^*$(b $^3\sum_u^+$) e+H$_2^*$(a $^3\sum_g^+$) e+ H$_2^*$(c $^3\prod_u^+$)
6	dissociation	e+ H$_2$(X $^1\sum_g^+$)	e+H(1s)+H*(2s)
7	ionization	e+H$_2$(X $^1\sum_g^+$)	e+H$_2$(v)$^+$+e
8	dissociative recombination	e+H$_2^+$(0$\leqslant v\leqslant$9)	H(1s)+H*($n\geqslant$2)
9	dissociative recombination	e+H$_3^+$	H+H+H
10	elastic	e+ H$_2$	e+H$_2$

In order to discuss the spatial variation of the EEDF, the discharge volume can be divided into small spatial cells along the z direction as shown in Fig. 3. The figure shows the cross-sectional view in the x-z plane of the numerical cells used in the simulation.

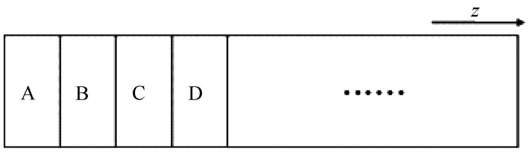

Fig. 3. Schematic for the division of the space.

Specifically, the electromagnetic force of the particle is solved inside A and B, and the field is interpolated on the grids by the volume weight; the particle information is updated by the effect of the field inside C, and the particle velocity is corrected by the calculation of the collisions; the particle emission and boundary condition are handled inside D, the influence of the plasma potential to the boundary particle is considered at the same time to confirm the balance of particles. During the process of the PIC-MCC algorithm, the process numbers of the particle information are extremely large. For the consideration of high operation efficiency, all the particle information is read from the hard disk at the start of a time step. And then the information is used to calculate the force and survival inside C and D respectively. Then the information is written into the buffer, which is directly used for the MCC collision. Finally, the new information is written back to the hard disk. As a result, the operation efficiency is enhanced by avoiding calling the hard disk frequently. Currently, solving the three dimensional Poisson equations is time consuming, and the electrostatic field has no significant effect on the multi-cusp ion source. Therefore the electrostatic field is ignored during the PIC-MCC simulation.

2.2 Permanent magnet calculation

The model of the single permanent magnet is shown in Fig. 4. The magnet has uniform magnetization along the z axis. The length, width, and height of the magnet are a, b, and h along the x, y, and z axes, respectively.

Based on the Biot and Savart law, the magnetostatic field is solved as follows [10]

$$B_x = -\frac{K}{2}[\Gamma(a-x,y,z)+\Gamma(a-x,b-y,z)-\Gamma(x,y,z) -\Gamma(x,b-y,z)]|_0^h, \tag{2}$$

$$B_y = -\frac{K}{2}[\Gamma(b-y,x,z)+\Gamma(b-y,a-x,z)-\Gamma(y,x,z) -\Gamma(y,a-x,z)]|_0^h, \tag{3}$$

$$B_z = -K[\phi(a-x,y,z)+\phi(b-y,a-x,z) +\phi(x,b-y,z)+\phi(a-x,b-y,z)+\phi(b-y,x,z) +\phi(y,x,z)+\phi(a-x,y,z)+\phi(x,y,z)]|_0^h, \tag{4}$$

where $K=\dfrac{\mu_0 j}{4\pi}$ is the hysteresis of the permanent magnet.

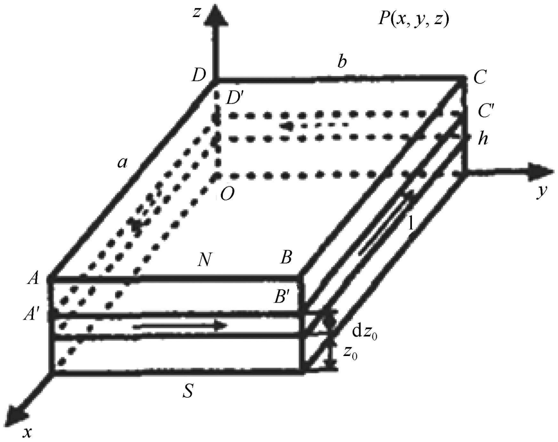

Fig. 4. Model of the single permanent magnet.

2.3 Boundary conditions

In order to take into account the sheath potential drop near walls and plasma grid, the simple model is used as follows. If the test electrons reach the boundary walls, those electrons with the energy E_e larger than the sheath potential drop ($E_e \geqslant eV_{sh}$) are absorbed at the wall, while those with the low energy ($E_e \geqslant eV_{sh}$) are reflected. The sheath potential drop V_{sh} can be estimated from the sheath theory [7].

$$V_{sh} = (kT_e/2e)\ln[(1/2\pi)\cdot(m_i/m_e)], \tag{5}$$

where T_e and m_i are the electron temperature and ion mass, respectively. In the simulation, T_e in Eq. (5) is given by the average energy of the test electrons in the cell closest to the wall.

3 Numerical simulations

3.1 Initial conditions

The PIC-MCC code is applied to analyze the multi-cusp proton source. The model and structure of the multi-cusp proton source are shown in Fig. 5, 14 Sm-Co permanent magnets are adopted in the simulation. There are 12 permanent magnets around the discharge chamber and 2 magnets on the top of the discharge chamber. The size of permanent magnet is by 17 mm×12 mm×100 mm and the surface remnant magnetic field $B_{\rm r}$=1.1 T. They all act as confinement magnets to confine the plasma. The structure of the discharge chamber is also shown in the figure. The chamber is made of stainless steel with an inner radius of 50 mm and a thickness of 4 mm. The mesh grids of the Δx, Δy, Δz direction are all of 1 mm. The numerical time step during the PIC Δt is equal to 10^{-11}s, which is much smaller than the Larmor period in the magnetic field. The time step $\Delta t_{\rm NC}$ and $\Delta t_{\rm BC}$ for the NC method and the BC method are all equal to 10^{-9}s. The former is much smaller than the minimum flight time of the NC method. The latter is chosen so as to simulate the important feature of the small angle scattering of the Coulomb collision.

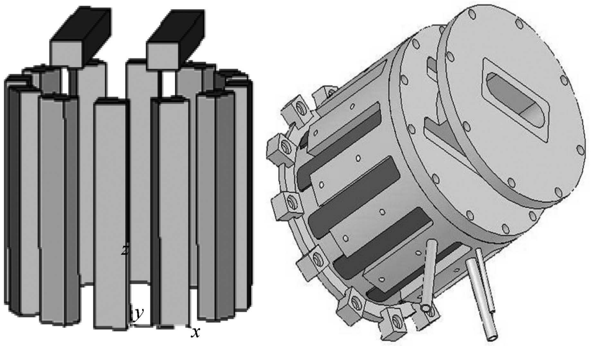

Fig. 5. The model and structure of the discharge chamber.

The typical design operation parameters of the multi-cusp proton source are as follows. The arc power, voltage, and gas pressure are 10 kW, 60 V, and 0.3 Pa, respectively. As a result, the initial energy of the primary electrons emitted from the filaments is set to be 60 eV, with the assumption that these electrons are accelerated by the thin sheath region surrounding the filaments immediately after thermal emission. For simplicity, the emitted angle is chosen from the isotropic distribution. The main collision process included in the simulation has already been shown in Table 1. The main simulation parameters related to the collision process with hydrogen particles are set as follows. The temperature of the hydrogen molecule is initially set to 300 K; the density ratio of the hydrogen molecule and the atom is 10 to 1; the densities of the H_2^+ and H_3^+ are 1×10^{17} m^{-3} and 5×10^{17} m^{-3}, respectively. And the densities of the hydrogen species are all uniform and unchanged during the simulation [11].

3.2 Numerical results

During the simulation, the time steps and collision processes are repeated until the electron density obtains a steady state. The electron density vs the simulation time is shown in Fig. 6. At the time 1.6×10^{-5} s, the electron becomes in a steady state. And the electron density reaches 0.95×10^{-17} m^{-3}.

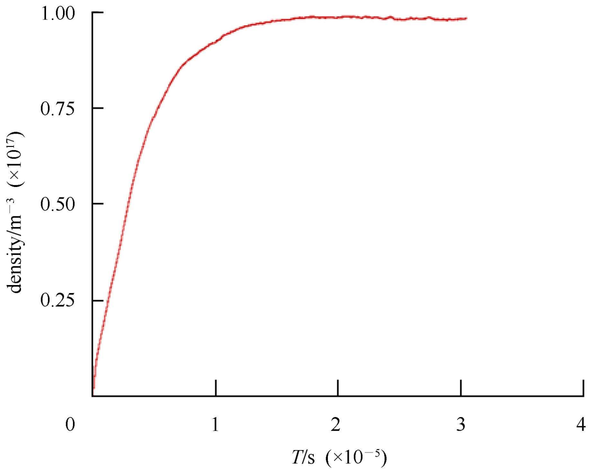

Fig. 6. The electron density vs the simulation time.

The electron energy distribution function (EEDF) is calculated during the simulation. The results are shown in Fig. 7. These electron temperatures are calculated by the linear fitting of the EEDF/$E^{1/2}$ (EEDF divided by $E^{1/2}$) vs E plot with the least squares method. The slope of the EEDF curve is the electron temperature. As shown in the figure, there are two temperature states of the electron inside the discharge chamber; the low temperature (the dotted line) and the high temperature (the solid line) are equal to 3.01 eV and 19.85 eV, respectively. They are meaningful for the volume production ion source. The high temperature electron is important to produce the excitation hydrogen molecule, while the low temperature electron is the key factor for the production of the proton in the extraction region. The total number of electrons is more than one hundred thousand, which can be satisfied by the statistical requirements.

The distributions of the electron phase space at the x=0, y=0 and z=60 mm planes are shown in Fig. 8. The plasma (both the electrons and the ions) is confined by the multi-cusp magnetic field around the discharge chamber. As discussed previously, the field-free region in the multi-cusp proton source is about 34 mm, where the electron is confined by the multi-cusp magnetic field [2]. It can be seen from Fig. 8 that the main distribution region of the

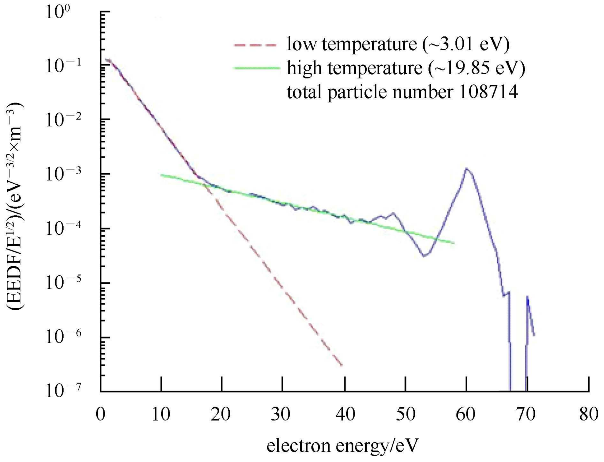

Fig. 7. The normalized electron energy distribution function vs the electron energy in the simulation space (log scale).

electron in the discharge chamber is about 36 mm. The electron distribution region is much close to the field free region. As a result, the design of the magnets for the discharge chamber is reasonable.

It also can be seen from Fig. 8 (a and b) that there is a drift of the dense electron distribution along the positive y direction. As shown in Fig. 8(d), due to the top two magnets of the discharge chamber, there is a gradient magnetic field along the z axis, which causes the $\vec{B}\times\nabla B$ along the minus y direction. As a result, the electron will have a drift along the positive y direction.

The electron energy distributions along the axes also have been monitored during the simulation. The results are shown in Fig. 9. It can be seen from Fig. 9(a) that the electron energy is uniform along the x axis. The high energy electron is absorbed by the walls, while the low energy electron is reflected by the walls. In Fig. 9(c), the electron is confined by the top multi-cusp magnetic field. As a result, there are a few low energy electrons confined at the top of the discharge chamber, while the majority of high energy

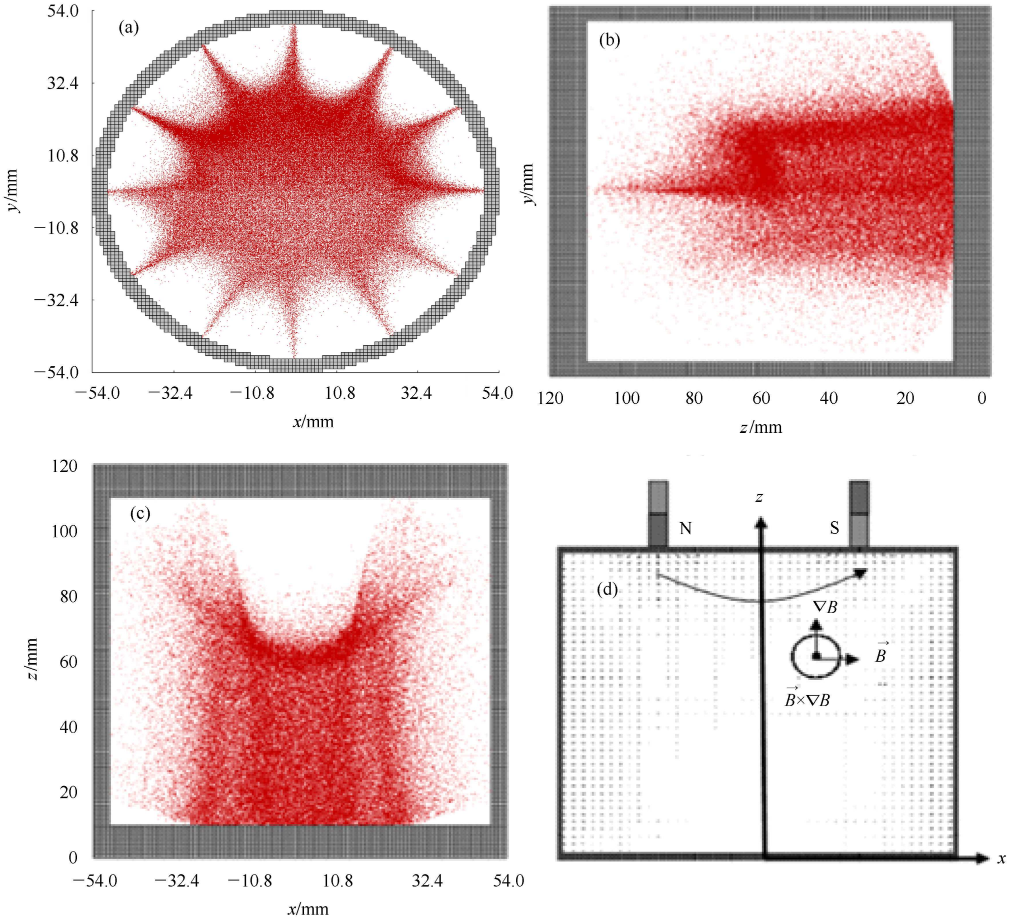

Fig. 8. Distribution of the electron phase space at different planes. (a) z=60 mm plane; (b) x=0 plane; (c) y=0 plane; (d) magnetic field distribution at y=0 plane.

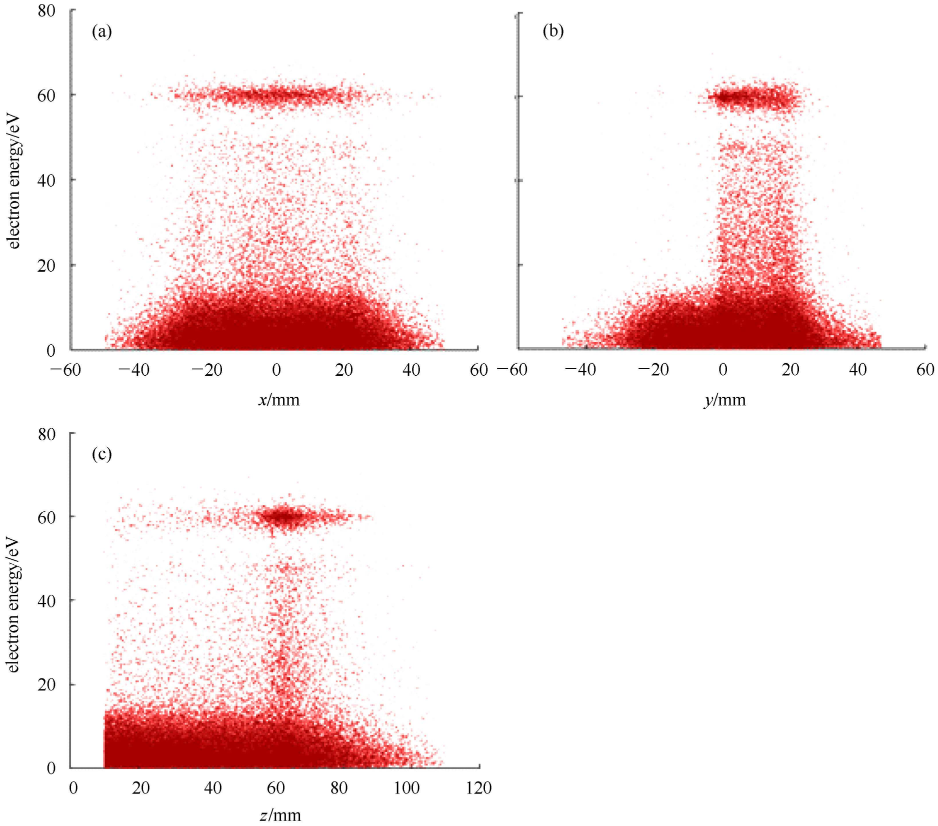

Fig. 9. The electron energy distributions along the axes. ((a) along the x axis; (b) along the y axis; (c) along the z axis).

electrons drift to the extraction region. Also it can be seen from Fig. 9(b) that there is a drift along the positive y direction especially for the high energy electron. The high energy electron drifts through the magnetic field more easily because the Larmor radius of the high energy electron is larger than the low one under an identical magnetic field given. Therefore, the drift of the high energy electron is observed.

4 Conclusion

The three dimensional PIC-MCC code is developed based on the CHIPIC particle simulation software. The code is successfully applied to analyze the multi-cusp proton source in CHIPIC. Previous studies focused on the design for the magnetostatic field and the optical of the extraction beam. The results of numerical simulations of the electron energy distribution for the multi-cusp proton source have proved that the design of the discharge chamber is reasonable. The simulation results also indicate that there are two electron temperature distributions inside the discharge chamber, and a spatial non-uniformity of the electron density along the positive y direction due to the $\vec{B}\times\nabla B$ drift. Future work will focus on the spatial uniformity of the plasma in the discharge chamber.

References

1 FANG S X, GUAN X L, TANG J Y. Chinese Physics C (HEP & NP), 2010, **34**(3): 383–388

2 WU X B, HUANG T, OUYANG H F et al. Chinese Physics C (HEP & NP), 2010, **34**(12): 1900–1904

3 LIU D G, ZHU D J, ZHOU J et al. High Power Laser and Particle Beams, 2006, **18**(1): 110–114 (in Chinese)

4 WANG X M, YANG C, LIU D G et al. High Power Laser and Particle Beams, 2011, **23**(10): 2767–2772 (in Chinese)

5 Verboncoeur J P. Plasma Physics and Controlled Fusion, 2005, **47**(5A): A231–A260

6 Birdsall C K, Langdon A B. Plasma Physics via Computer Simulation. New York: McGraw-Hill, 1985

7 Terasaki R, Hatayama A, Shibata T et al. AIP Conference Proceedings, 2011, **1390**(1): 22–29

8 Takizuka T, Abe H. Journal of Computational Physics, 1977, **25**(3): 205–219

9 Nanbu K. IEEE Transactions on Plasma Science, 2000, **28**(3): 971–990

10 GOU X F, YANG Y, ZHEN X J. Applied Mathematics and Mechanics, 2004, **25**(3): 271–278 (in Chinese)

11 Katoh K, Takado N, Hatayama A et al. Review of Scientific Instruments, 2006, **77**(3): 03A535–533